10-2020

Charge Trapping by Iodine Ions in Photorefractive $Sn_2P_2S_6$ Crystals

Elizabeth M. Scherrer
Air Force Institute of Technology

Nancy C. Giles
Air Force Institute of Technology

Tabitha E. R. Dodson
Air Force Institute of Technology

A. A. Grabar
Uzhgorod National University - Ukraine

D. R. Evans
Air Force Research Laboratory

See next page for additional authors

Recommended Citation

E. M. Scherrer, N. C. Giles, T. E. R. Dodson, A. A. Grabar, D. R. Evans, S. A. Basun, J. E. Slagle, and L. E. Halliburton , "Charge trapping by iodine ions in photorefractive Sn2P2S6 crystals", J. Chem. Phys. 153, 144503 (2020) https://doi.org/10.1063/5.0025541

The Journal of Chemical Physics

Charge trapping by iodine ions in photorefractive $Sn_2P_2S_6$ crystals

Cite as: J. Chem. Phys. **153**, 144503 (2020); https://doi.org/10.1063/5.0025541
Submitted: 16 August 2020 • Accepted: 25 September 2020 • Published Online: 13 October 2020

E. M. Scherrer, N. C. Giles, T. E. R. Dodson, et al.

The Journal of Chemical Physics ARTICLE scitation.org/journal/jcp

Charge trapping by iodine ions in photorefractive $Sn_2P_2S_6$ crystals

Cite as: J. Chem. Phys. 153, 144503 (2020); doi: 10.1063/5.0025541
Submitted: 16 August 2020 • Accepted: 25 September 2020 •
Published Online: 13 October 2020

E. M. Scherrer,[1] N. C. Giles,[1] T. E. R. Dodson,[1,2] A. A. Grabar,[3] D. R. Evans,[4] S. A. Basun,[4,5] J. E. Slagle,[4] and L. E. Halliburton[5,6,a)]

AFFILIATIONS

[1]Department of Engineering Physics, Air Force Institute of Technology, Wright-Patterson Air Force Base, Ohio 45433, USA
[2]Gryphon Schafer, Arlington, Virginia 22203, USA
[3]Institute for Solid State Physics and Chemistry, Uzhhorod National University, 88000 Uzhhorod, Ukraine
[4]Air Force Research Laboratory, Materials and Manufacturing Directorate, Wright-Patterson Air Force Base, Ohio 45433, USA
[5]Azimuth Corporation, 2970 Presidential Drive, Suite 200, Fairborn, Ohio 45324, USA
[6]Department of Physics and Astronomy, West Virginia University, Morgantown, West Virginia 26506, USA

[a)]**Author to whom correspondence should be addressed:** Larry.Halliburton@mail.wvu.edu

ABSTRACT

Electron paramagnetic resonance (EPR) is used to establish the role of iodine as an electron trap in tin hypothiodiphosphate ($Sn_2P_2S_6$) crystals. Iodine ions are unintentionally incorporated when the crystals are grown by the chemical-vapor-transport method with SnI_4 as the transport agent. The $Sn_2P_2S_6$ crystals consist of Sn^{2+} ions and $(P_2S_6)^{4-}$ anionic groups. During growth, an iodine ion replaces a phosphorus in a few of the anionic groups, thus forming $(IPS_6)^{4-}$ molecular ions. Following an exposure at low temperature to 633 nm laser light, these $(IPS_6)^{4-}$ ions trap an electron and convert to EPR-active $(IPS_6)^{5-}$ groups with S = 1/2. A concentration near 1.1×10^{17} cm^{-3} is produced. The EPR spectrum from the $(IPS_6)^{5-}$ ions has well-resolved structure resulting from large hyperfine interactions with the ^{127}I and ^{31}P nuclei. Analysis of the angular dependence of the spectrum gives principal values of 1.9795, 2.0123, and 2.0581 for the g matrix, 232 MHz, 263 MHz, and 663 MHz for the ^{127}I hyperfine matrix, and 1507 MHz, 1803 MHz, and 1997 MHz for the ^{31}P hyperfine matrix. Results from quantum-chemistry modeling (unrestricted Hartree–Fock/second-order Møller–Plesset perturbation theory) support the $(IPS_6)^{5-}$ assignment for the EPR spectrum. The transient two-beam coupling gain can be improved in these photorefractive $Sn_2P_2S_6$ crystals by better controlling the point defects that trap charge.

I. INTRODUCTION

In addition to serving as a model system for complex ferroelectric behavior,[1–3] tin hypothiodiphosphate ($Sn_2P_2S_6$, or simply SPS) is a photorefractive semiconductor with fast response times and high gain factors in the visible and near-infrared.[4–17] A transient peak in the temporal dynamics of the two-beam coupling in this material has been attributed to contributions from two types of movable charges.[6,12,13] A fast grating is formed by optically excited charge carriers, while a slower grating appears because of a redistribution of thermally excited (optically inactive) carriers of opposite sign. These space-charge gratings are out-of-phase and thus compensate each other. The different characteristic build-up times for the two gratings lead to an initial peak in the two-beam coupling and then a decrease within tens of seconds to a lower steady-state value. Another important feature of the photorefractive effect in some SPS crystals is the enhancement caused by optical sensitizing (i.e., exposing a crystal to light in the 530–675 nm range before writing a grating).[4,13,14]

To increase the two-beam coupling and also to explain variations in the photorefractive response observed among SPS crystals grown at different times and by different methods, all the point defects that may serve as traps for photoexcited electrons and holes in this highly compensated semiconductor need to be

identified. Electron paramagnetic resonance (EPR), with its narrow linewidths and high sensitivity, is a suitable experimental technique to explore the wide range of intrinsic and extrinsic point defects that can be present in SPS crystals.[18–20] Exposure to appropriate wavelengths of light allows electrons and holes to be redistributed among the donors and acceptors that are introduced during growth. Self-trapping of charge may also occur. At all times, the crystal will remain electrically neutral. This redistribution of charge as a result of illumination, although stable at low temperatures, will be transient at room temperature and forms the basis of the photorefractive effect. Thus far, photoinduced EPR has been used to identify hole-like small polarons (Sn^{3+}),[21] electron-like small polarons (Sn^{+}),[17] singly ionized sulfur vacancies,[22] singly ionized tin vacancies,[23] and two Sb-related defects.[24–26] In each case, the resolved hyperfine structure in the EPR spectrum provides the critical information that allows a specific defect model to be assigned.[27]

In the present paper, we investigate the charge-trapping role of iodine ions in an SPS crystal. This crystal was unintentionally doped with iodine (as a result of the growth method) and, at the same time, was deliberately doped with tellurium. Recent work shows that the Te ions replace Sn and S ions and thus provide both electron and hole trapping sites that are active during an illumination.[28] This leaves the important question: What site (Sn, P, or S) does an iodine ion occupy in an SPS crystal? Iodine is often found in crystals as a negative ion (I^-) with the $[Kr]4d^{10}5s^25p^6$ closed-shell configuration. An example from the alkali halide family is sodium iodide (NaI), a widely used scintillator material. There are other examples, such as the well-known nonlinear optical crystal $LiIO_3$, where iodine is a positive ion (I^{5+}) with the $[Kr]4d^{10}5s^2$ closed-shell configuration. Our initial expectation was that an iodine ion in SPS would act the same as Te ions and occupy a S or Sn site. However, neither of these sites (S or Sn) for the iodine ions is supported by our present EPR data. Instead, our observation of a very large hyperfine interaction with only one ^{31}P nucleus indicates that iodine ions in SPS crystals occupy a phosphorous site and can trap an electron following an illumination at low temperature with sub-bandgap laser light. Before light, the iodine is part of a nonparamagnetic $(IPS_6)^{4-}$ molecular ion (i.e., no unpaired spins). After light, the extra electron converts this molecular ion to a paramagnetic $(IPS_6)^{5-}$ unit. A complete set of EPR angular dependence data for the ^{127}I and ^{31}P hyperfine interactions, coupled with predictions of Fermi contact parameters and spin density distribution from quantum chemistry calculations, support this $(IPS_6)^{5-}$ model for an electron trapped by an iodine ion in SPS crystals.

II. CRYSTAL STRUCTURE AND BONDING

A ferroelectric–paraelectric phase change occurs at 64 °C in $Sn_2P_2S_6$ crystals. Below this temperature, the crystals are monoclinic with space group *Pc* (No. 7) and point group *m*. Lattice constants at room temperature[29,30] are $a = 9.378$ Å, $b = 7.488$ Å, $c = 6.513$ Å, and $\beta = 91.15°$. The *b* axis is perpendicular to the mirror plane of the crystal, and β is the angle between the *a* and *c* directions. When analyzing the angular dependence of the EPR spectrum, the crystal is treated as orthorhombic and the slight deviation from 90° between the *a* and *c* axes is ignored. Both covalent and ionic behaviors occur in the $Sn_2P_2S_6$ crystals. As shown in Fig. 1, the building blocks for constructing an SPS crystal are Sn^{2+} ions and $(P_2S_6)^{4-}$ molecular ions. The Sn^{2+} ions have a significant ionic nature, whereas the $(P_2S_6)^{4-}$ anionic groups have strong covalent P–P and P–S bonds.[31–33] There are no unpaired spins in these Sn^{2+} ions and $(P_2S_6)^{4-}$ groups. In the low-temperature ferroelectric phase of this material, there are two slightly inequivalent tin sites, two slightly inequivalent phosphorous sites, and six inequivalent sulfur sites. Above 64 °C, in the paraelectric phase, the two tin sites are equivalent and the two phosphorous sites are equivalent, but the sulfur sites remain inequivalent.[30]

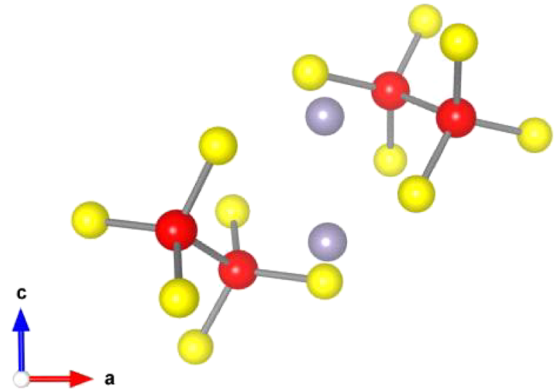

FIG. 1. A schematic representation of an $Sn_2P_2S_6$ crystal. The basic building blocks of the crystal are Sn^{2+} ions and $(P_2S_6)^{4-}$ molecular ions. This view is looking along the *b* direction. The phosphorous ions are red, the sulfur ions are yellow, and the tin ions are gray.

III. EXPERIMENTAL DETAILS

The $Sn_2P_2S_6$ crystal used in the present investigation was grown at Uzhhorod University by the chemical vapor transport method using SnI_4 as the transport agent.[34,35] A small portion of the iodine from the carrier gas entered the growing crystal. This is an expected effect, with ZnSe providing an early example of unintentional doping by the iodine transport agent during chemical vapor transport growth.[36,37] In addition to the inadvertent incorporation of iodine, our SPS crystal was deliberately doped during growth by adding 1% (by weight) of tellurium to the starting materials. These tellurium ions play a direct role, at low temperatures, in allowing electrons to be trapped at iodine ions. The sample for the EPR experiments, cut from the larger as-grown boule, was rectangular in shape with the *a*, *b*, and *c* axes normal to the faces. Dimensions were ~2 mm on a side.

A Bruker EMX spectrometer, operating near 9.39 GHz, was used to take the EPR spectra. The sample temperature was controlled by adjusting the flow of cold helium gas through an Oxford Instruments ESR-900 cryostat attached to a Bruker ER4103TM cylindrical microwave cavity. A helium–neon laser (producing 12 mW at 633 nm) was used to convert defects within the crystal to their paramagnetic charge states. The optical absorption edge of SPS crystals is near 530 nm at room temperature[38] and shifts to 500 nm for temperatures below 100 K.[39]

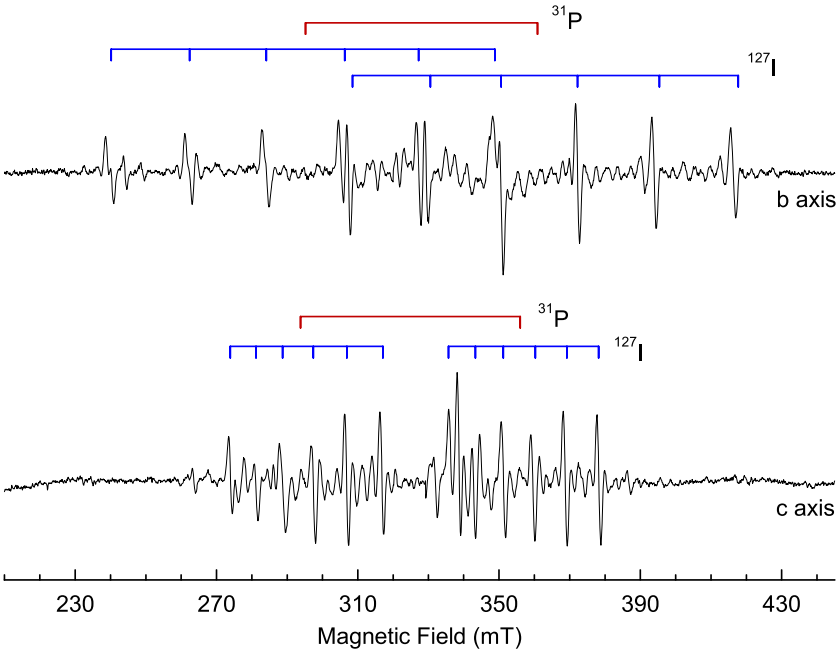

FIG. 2. EPR spectra of an iodine-related defect in an $Sn_2P_2S_6$ crystal, taken at 20 K with a microwave frequency of 9.39 GHz. The magnetic field is along the *b* direction in the upper spectrum and along the *c* direction in the lower spectrum. Stick diagrams above the spectra identify the lines due to ^{127}I and ^{31}P nuclei.

IV. RESULTS

A. Iodine-related EPR spectra

Figure 2 shows two EPR spectra from the iodine-related trapped electron defect in our $Sn_2P_2S_6$ crystal. They were both taken at 20 K, with the magnetic field along the *b* direction in the upper spectrum and along the *c* direction in the lower spectrum. The multi-step process used to produce this new defect in the Te-doped sample is described in Sec. IV D. Each spectrum in Fig. 2 consists of two sets of six lines, with stick diagrams above the spectra identifying individual lines within each set. Based on a comparison to an EPR pitch sample provided by Bruker, our estimate of the concentration of defects responsible for the spectra in Fig. 2 is 1.1×10^{17} cm^{-3}.

The hyperfine patterns observed in Fig. 2, i.e., two sets of six lines, suggest that the responsible defect has one unpaired electron spin (S = 1/2) interacting with two nuclear spins (I = 1/2 and I = 5/2). Both the I = 1/2 nucleus and the I = 5/2 nucleus must be very near 100% abundant because there are no observable I = 0 lines in the spectra in Fig. 2. Obvious choices for these nuclei are ^{31}P and ^{127}I. Phosphorus is a constituent of $Sn_2P_2S_6$ crystals; thus, it is reasonable to assign the I = 1/2 interaction to the 100% abundant ^{31}P nuclei. Other possible 100% abundant I = 1/2 nuclei are ^{1}H, ^{19}F, ^{89}Y, ^{103}Rh, ^{169}Tm, and combined ^{203}Tl and ^{205}Tl. These latter two isotopes have I = 1/2, with similar magnetic moments, and together appear as 100% abundant. The hyperfine parameters (isotropic Fermi contact and anisotropic dipole–dipole) determined in Sec. IV B for the I = 1/2 interaction are larger than the predicted maximum values[40,41] for ^{1}H, ^{89}Y, and ^{103}Rh, thus removing these nuclei from consideration. Fluorine, thulium, and thallium, as well as yttrium and rhodium, are not expected to be unintentionally present in our SPS crystal at the ~1×10^{17} cm^{-3} concentration level measured for our EPR spectrum.

The I = 5/2 nucleus contributing to the spectra in Fig. 2 must be extrinsic in origin since there are no isotopes of Sn and S that have I = 5/2. Possible assignments for this nucleus include ^{27}Al, ^{55}Mn, ^{127}I, ^{141}Pr, and combined ^{185}Re and ^{187}Re, as they are the only isotopes with I = 5/2 and 100% abundance. Of these, ^{127}I is the only realistic candidate since aluminum, praseodymium, and rhenium are not expected to be significant residual impurities in SPS crystals. A quite different EPR spectrum with S = 5/2 has already been assigned to Mn^{2+} ions occupying Sn^{2+} sites in Mn-doped $Sn_2P_2S_6$ crystals,[42] thus eliminating manganese from consideration. The use of the iodine-containing carrier gas during the chemical-vapor-transport growth of our crystal greatly strengthens the assignment of the I = 5/2 hyperfine lines in Fig. 2 to ^{127}I nuclei. Furthermore, a search of the literature reveals a series of previously reported EPR spectra that show similar resolved hyperfine patterns from ^{127}I nuclei.[43–48]

Numerous less intense EPR lines are present in the spectra in Fig. 2, in addition to the two intense sets of six lines identified by the stick diagrams. The majority of these smaller lines, located between the larger lines, are attributed to partially allowed transitions ($\Delta m_I = \pm 1$ and $\Delta m_I = \pm 2$) arising from a nuclear electric quadrupole interaction for the ^{127}I nuclei.[46,48,49] In general, the strength of a quadrupole interaction depends on the product of the electric quadrupole moment of the nucleus and the electric field gradient at the nucleus. The ^{127}I nucleus has a large quadrupole moment,[50] and the electric field gradients at nuclei in the low-symmetry monoclinic SPS crystals are also large; thus, significant nuclear electric quadrupole effects are expected in the iodine EPR spectra. A few lines in the 330–350 mT region of the spectra are assigned to holes trapped at Te ions on S sites,[28] electrons trapped at S vacancies,[22] and holes trapped at Sn vacancies.[23]

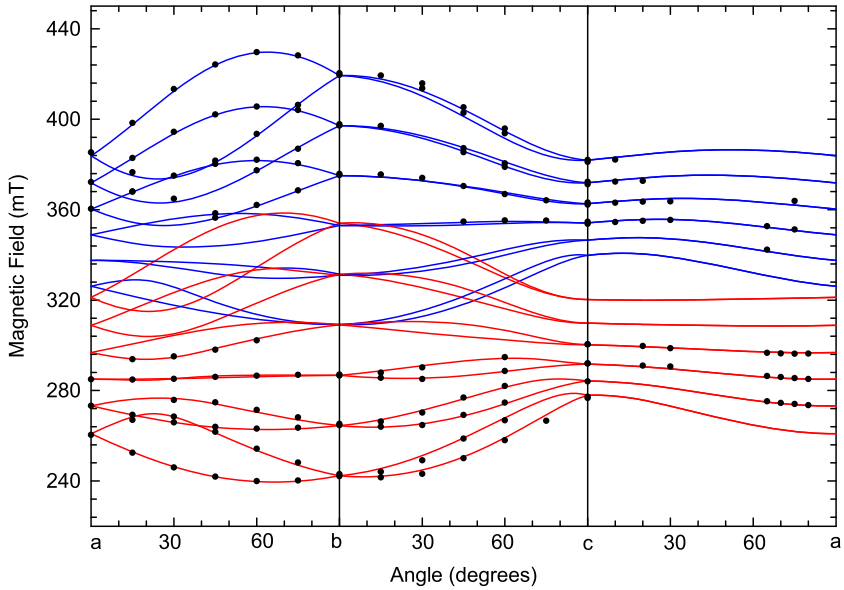

FIG. 3. Angular dependence of the EPR spectrum from the iodine-related defect. The magnetic field direction is rotated from *a* to *b*, *b* to *c*, and *c* to *a*.

B. Spin-Hamiltonian parameters

Complete sets of angular dependence data were taken for the iodine-related defect. These results, shown in Fig. 3, provide information about the *g* matrix and the ^{127}I and ^{31}P hyperfine matrices. The positions of the EPR lines, plotted as discrete points in Fig. 3, were acquired in three planes (*a*–*b*, *b*–*c*, and *c*–*a*), as the crystal was rotated relative to a fixed direction of the magnetic field. Overlapping of lines made it difficult to precisely locate the positions of lines near the centers of the spectra. In addition, in the *c*–*a* plane, locating the positions of the allowed lines was more challenging because of the increased intensities of nuclear-quadrupole-related partially allowed lines. When the ^{127}I hyperfine interaction becomes smaller relative to the nuclear quadrupole interaction (as it does in the *c*–*a* plane), the "forbidden" lines become more intense.

In the monoclinic structure of the SPS crystal, with the *b* axis normal to the mirror plane, a paramagnetic point defect can have two crystallographically equivalent orientations, i.e., sites. These two physically different orientations of the same defect, at different locations within the crystal, are related to each other by the symmetry elements of the crystal (in the present case, the mirror plane) and thus are crystallographically equivalent. The two defect orientations will have the same set of principal values, but a different set of principal-axis directions for each matrix in the spin Hamiltonian (see the next paragraph). The direction of the external applied magnetic field relative to the principal-axis directions of these matrices determines the positions (and spacings) of lines in the EPR spectrum for each orientation. When the two orientations are said to be magnetically equivalent, their EPR spectra are identical (i.e., they overlap). They separate into two similar, but easily distinguished, spectra when the two orientations are magnetically inequivalent. In our SPS crystal, the two crystallographically equivalent orientations of the iodine-related defect are magnetically equivalent when the magnetic field is along the *a*, *b*, or *c* directions, and they are also magnetically equivalent for all angles when the magnetic field is rotated in the *a*–*c* plane. In Fig. 3, as expected, there is a splitting into two branches in the *a*–*b* and *b*–*c* planes, but no splitting in the *a*–*c* plane.

The following spin Hamiltonian describes the EPR angular dependence shown in Fig. 3,

$$H = \beta \mathbf{S}\cdot\mathbf{g}\cdot\mathbf{B} + \mathbf{I_1}\cdot\mathbf{A_1}\cdot\mathbf{S} + \mathbf{I_2}\cdot\mathbf{A_2}\cdot\mathbf{S} - g_{n,1}\beta_n\mathbf{I_1}\cdot\mathbf{B} - g_{n,2}\beta_n\mathbf{I_2}\cdot\mathbf{B}. \quad (1)$$

An electron Zeeman term is included, along with hyperfine and nuclear Zeeman terms for the two nuclei (subscript 1 refers to the ^{127}I nucleus and subscript 2 refers to the ^{31}P nucleus). Here, **S**, $\mathbf{I_1}$, and $\mathbf{I_2}$ are the spin operators and **B** is the external magnetic field. The electron and nuclear Bohr magnetons are β and β_n, respectively. Each matrix (**g**, $\mathbf{A_1}$, and $\mathbf{A_2}$) in Eq. (1) has six independent parameters: three principal values and three Euler angles that describe the principal-axis directions. The values for these parameters were determined by fitting the experimental results in Fig. 3.

The spin Hamiltonian in Eq. (1), after being rewritten as a 24 × 24 matrix (S = 1/2, I_1 = 5/2, and I_2 = 1/2), was repeatedly diagonalized as the 18 parameters were systematically varied during a least-squares fitting process. Input data for the fitting were the 290 magnetic field values corresponding to the discrete points in Fig. 3. There are two sets of parameters that give equally good fits if only data from the *a*–*b*, *b*–*c*, and *c*–*a* planes are used. We determined the correct set by collecting additional data from *b* to the midpoint between *a* and *c*. The final best-fit values for the spin-Hamiltonian parameters are listed in Table I. Positive signs are assigned to the principal values of the hyperfine matrices, as the magnetic moments of the ^{31}P and ^{127}I nuclei are positive. For each matrix, the set of three Euler angles describing the principal-axis directions has been converted to three (θ, ϕ) pairs. The polar angle θ is defined relative to the *c* axis of the crystal, and the azimuthal angle ϕ is defined relative to the *a* axis with positive rotation being from *a* toward *b* in the plane perpendicular to *c*. In Table I, the principal-axis directions are

TABLE I. Spin-Hamiltonian parameters for the iodine-related defect in a $Sn_2P_2S_6$ crystal. Units for the principal hyperfine parameters are MHz. Uncertainties are estimated to be ±0.0005 for the *g* values, ±3.0 MHz for the A values, and ±3° for the angles.

		Principal-axis directions	
Principal values		θ (deg)	ϕ (deg)
g matrix			
g_1	1.9795	62.7	298.4
g_2	2.0123	27.4	113.3
g_3	2.0581	87.9	207.3
$\mathbf{A}_1$ hyperfine interaction (^{127}I interaction)			
A_1	232	16.6	210.0
A_2	263	106.4	200.4
A_3	663	92.6	291.1
$\mathbf{A}_2$ hyperfine interaction (^{31}P interaction)			
A_1	1507	54.0	221.8
A_2	1803	36.1	43.9
A_3	1997	91.0	132.6

for one of the two crystallographically equivalent orientations of the defect. Directions for the other orientation are obtained by applying a reflection through the mirror plane of the crystal. In Fig. 3, the solid lines were generated using the final best-fit values for the spin Hamiltonian parameters from Table I. The good agreement between the calculated curves and the discrete experimental points in Fig. 3 verifies that the correct set of spin-Hamiltonian parameters has been determined.

The principal-axis directions for the *g* matrix and the ^{31}P hyperfine matrix in Table I are not near the P–P or P–S bond directions in the crystal. The direction of the unique principal axis (A_3) of the ^{127}I hyperfine matrix, however, is reasonably close to the P–P bond direction. The θ and ϕ values in Table I for A_3 are 92.6° and 291.1°, and the corresponding θ and ϕ values for the P–P interatomic axis obtained from Ref. 29 are 110.9° and 307.8°. The Δθ and Δϕ differences are 18.3° and 16.7°, respectively.

C. Defect model

A large hyperfine interaction with only one phosphorous nucleus is the critical feature in the EPR spectrum that allows a model to be proposed for the iodine-related defect. In the regular SPS lattice, phosphorous ions are always present as pairs, adjacent to each other in the $(P_2S_6)^{4-}$ anionic groups (see Fig. 1). Earlier EPR studies of defects in SPS crystals have verified this pairing by showing equal, or nearly equal, hyperfine interactions with two phosphorous nuclei.[22,23,25] The large phosphorous interaction in our present spectra indicates that a P_2S_6 unit must be involved, but the lack of a resolved interaction with a second phosphorous nucleus strongly suggests that one of the two phosphorous ions has been replaced by another ion. Iodine, with its I = 5/2 nuclear spin, is the obvious choice for the ion that replaces a phosphorus. A small fraction of the regular $(P_2S_6)^{4-}$ molecular ions are replaced by $(IPS_6)^{4-}$ units in the as-grown crystal (see Fig. 4). The original $(P_2S_6)^{4-}$ groups are

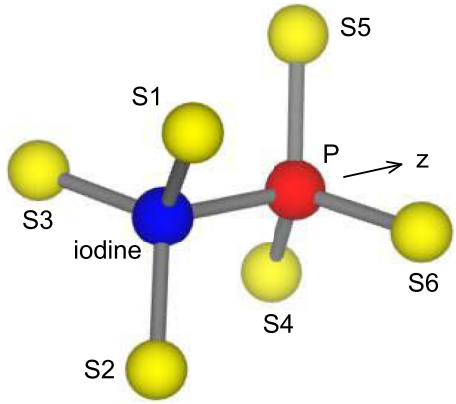

FIG. 4. The eight-ion $(IPS_6)^{5-}$ cluster used in the quantum chemistry modeling of the iodine-related defect in $Sn_2P_2S_6$. Iodine is blue, phosphorous is red, and the sulfur ions are yellow. The ion positions are given in Table III.

not paramagnetic (i.e., have no unpaired spins), and the $(IPS_6)^{4-}$ units also are not paramagnetic. When an electron is trapped at low temperatures as a result of illumination, these latter units convert to paramagnetic $(IPS_6)^{5-}$ units with S = 1/2. The large phosphorous hyperfine interaction strongly supports that an electron, instead of a hole, is trapped at the $(IPS_6)^{4-}$ unit. A hole would be more localized on the sulfur ions and thus give a smaller ^{31}P interaction.

The experimental spin Hamiltonian parameters in Table I provide information about the distribution of the unpaired spin within the $(IPS_6)^{5-}$ molecular ion. Each hyperfine matrix can be separated into an isotropic part *a* and an anisotropic part **B**, with **U** being the identity matrix,

$$\mathbf{A} = a\mathbf{U} + \mathbf{B}. \tag{2}$$

The Fermi contact interaction, proportional to the unpaired spin density ρ_s at the nucleus, is represented by the scalar *a*, while the angular-dependent magnetic dipole–dipole coupling between the unpaired electron and the nucleus is represented by the traceless matrix **B**,[18–20]

$$a = \frac{2}{3}\mu_0 g\beta g_n\beta_n\langle\rho_s(r=0)\rangle, \tag{3}$$

$$B_{ij} = \frac{\mu_0}{4\pi}g\beta g_n\beta_n\int\left(\frac{3x_ix_j}{r^5} - \frac{\delta_{ij}}{r^3}\right)\langle\rho_s(r)\rangle dV. \tag{4}$$

The hyperfine matrices **A**, from Eq. (2), are rewritten in the following form:

$$\mathbf{A} = \begin{pmatrix} a & 0 & 0 \\ 0 & a & 0 \\ 0 & 0 & a \end{pmatrix} + \begin{pmatrix} -b+b' & 0 & 0 \\ 0 & -b-b' & 0 \\ 0 & 0 & 2b \end{pmatrix}. \tag{5}$$

Here, *b* is the axial part of the dipole–dipole interaction and *b*′ describes the deviation from axial symmetry. Table II gives the values for *a*, *b*, and *b*′ obtained from the ^{127}I and ^{31}P hyperfine matrices in Table I.

TABLE II. Experimental Fermi contact (a) and dipole–dipole (b and b') parameters for the iodine-related defect in $Sn_2P_2S_6$ [see Eqs. (2)–(5) for the definition of a, b, and b']. These values are taken from the ^{127}I and ^{31}P hyperfine matrices in Table I. Units for the a, b, and b' parameters are MHz.

Nucleus	a	b	b′
^{127}I	386	139	−15
^{31}P	1769	114	−148

The results for b and b' in Table II show that the anisotropic ^{127}I hyperfine interaction is axial (b' is much less than b). This is consistent with the unique (A_3) principal-axis direction for ^{127}I in Table I being close to the P–P direction (or for our model, the I–P direction). In other words, a major portion of the unpaired spin density contributing to the dipole–dipole interaction for the ^{127}I nucleus is distributed symmetrically about the I–P direction. In contrast, Table II shows that the anisotropic ^{31}P interaction is strongly nonaxial (b' is greater than b). This suggests that a significant portion of the unpaired spin density on the phosphorus may be in a p-type orbital oriented perpendicular to the I–P axis. There will also be spin density located along the I–P direction between the iodine and phosphorus and around the iodine. Having the spin density distributed in two orthogonal directions about the ^{31}P nucleus will result in a dipole–dipole interaction that is strongly nonaxial, in agreement with the b and b' values reported for this nucleus in Table II.

Reference atomic values, obtained from *ab initio* calculations, are available to help interpret hyperfine parameters.[40,41] They are often used to analyze the unpaired spin composition of a defect in terms of s and p orbitals. This approach provides a rudimentary, but useful, picture of the ground state of a defect. For the ^{31}P nucleus, Fitzpatrick *et al.*[41] predicted that a 100% occupied phosphorous 3s orbital has a Fermi contact value of 10 201 MHz. Our experimental value of 1769 MHz for a from Table II, when compared with this prediction, suggests that 17.3% of the unpaired spin in the $(IPS_6)^{5-}$ defect is in a phosphorous 3s orbital. Similarly, a comparison of our experimental value of 114 MHz to the value of 316.7 MHz (2/5 of 791.7 MHz) predicted by Fitzpatrick *et al.*[41] for the phosphorous anisotropic (dipolar) parameter b suggests that 36.0% of the unpaired spin in the defect is in a phosphorous 3p orbital. The angular factor of 2/5 is used in this determination of the 3p contribution.[40]

Morton and Preston[40] provided the only reference atomic values in the literature for the ^{127}I nucleus. They predicted that a 100% occupied iodine 5s orbital has a Fermi contact value of 41 600 MHz and a 100% occupied iodine 5p orbital has a value of 812 MHz (2/5 of 2031 MHz). Our experimental value of 386 MHz for a suggests that 0.9% of the unpaired spin is in an iodine 5s orbital, and our value of 139 MHz for b suggests that 17.1% is in an iodine 5p orbital. Fitzpatrick *et al.*[41] suggested that the early predictions of Morton and Preston[40] should be lowered by 20% because of approximations made when implementing the Hartree–Fock method. This may especially be the case for the "heavier" atoms in the Periodic Table such as iodine. Thus, we expect that our percentages of 5s and 5p contributions to the $(IPS_6)^{5-}$ group should be increased by at least 20%.

The general conclusions from this cursory analysis of the experimental hyperfine parameters are that ~50% of the unpaired spin is centered on the participating phosphorous ion, about 20% is associated with the iodine ion, and the remainder is distributed over the six neighboring sulfur ions. The only isotope of sulfur that has a nonzero nuclear spin (^{33}S with I = 3/2) is just 0.75% abundant, and thus, its hyperfine lines are too weak to detect in the EPR spectra.

D. Defect production

Several steps were involved in producing the specific charge state of the defect responsible for the EPR spectra in Fig. 2. There were no EPR signals detected after the crystal was initially cooled to 20 K while being kept in the dark. The crystal was then exposed at 20 K to sub-bandgap 633 nm laser light for 5 min. This exposure did not, by itself, form the iodine-related defects seen in Fig. 2, and another step was needed for their production. After removing the light, the crystal was warmed to near 100 K and held there for 2 min. Then, the crystal was immediately returned to 20 K where the spectra shown in Fig. 2 were recorded.

A large number of Te ions deliberately added to the crystal during growth play an important role in the production of the iodine-related EPR spectrum. During the initial illumination at 20 K, holes are trapped at Te ions substituting for S ions and electrons are trapped at Te ions substituting for Sn ions. Detailed descriptions of the EPR spectra from these Te-related defects have been reported.[28] Nonparamagnetic Te^{4+} ($5s^2$) ions that replace Sn^{2+} ($5s^2$) ions during growth trap two electrons and form Te^{2+} ($5s^25p^2$) ions during the exposure to laser light at 20 K. Then, when the crystal is warmed in the dark to near 100 K, the two trapped electrons are thermally released from the Te^{2+} ions. This restores the Te^{4+} ions. Many of the released electrons annihilate holes trapped by Te ions at S sites, but a significant portion moves to iodine ions occupying phosphorous sites and forms the S = 1/2 iodine-related defect responsible for the EPR spectra in Fig. 2. Although the EPR signal for the iodine defect is easily produced at 100 K in Te-doped SPS, it slowly decays over several minutes when the crystal is subsequently held constant near 50 K. To prevent thermal decay of the signal, the crystal was always quickly cooled back to 20 K after the 100 K production step.

Trapping of electrons by iodine has also been observed in an SPS crystal that did not contain tellurium ions,[21] thus demonstrating the broader significance of our present study. The three highest field lines in our iodine related EPR spectrum when the magnetic field is along the b direction (see the upper spectrum in Fig. 2) correspond directly to the very weak lines near 375 mT, 397 mT, and 419 mT in Fig. 2 in Ref. 21. The defect responsible for these lines was not identified in that early work. However, as a result of the current investigation, they can now be assigned to electrons trapped by iodine ions. The iodine spectrum in Ref. 21 was produced at 25 K with 442 nm light in an SPS crystal doped with Ag, with hole-like small polarons and possibly Ag ions on Sn sites serving as the defects that trap the compensating holes. This Ag-doped crystal was grown at Uzhhorod University by the chemical vapor transport method using SnI_4 as the transport agent.

TABLE III. Positions of the eight ions comprising the $(IPS_6)^{5-}$ cluster used in the UHF/UMP2 modeling. These positions are generated from the $Sn_2P_2S_6$ structural information in Ref. 29. The iodine ion is located at the origin, and the z direction is defined to be along the I–P bond. Units are angstroms (Å).

Ion	x	y	z
I	0.0000	0.0000	0.0000
P	0.0000	0.0000	2.1924
S1	1.4920	1.2421	−0.5219
S2	−1.8613	0.6101	−0.5746
S3	0.2945	−1.9376	−0.4909
S4	−1.4826	−1.2181	2.8004
S5	1.8971	−0.5956	2.6996
S6	−0.2420	1.9352	2.7219

V. QUANTUM CHEMISTRY MODELING

A relatively simple quantum chemistry calculation supports our model of an $(IPS_6)^{5-}$ molecular ion for the EPR-active iodine-related defect in SPS. The eight-ion cluster in Fig. 4 is used, where the relative positions of the ions are the same as in the P_2S_6 groups in the regular crystal. One of the phosphorous ions is replaced by an iodine ion. The coordinates of the eight ions are given in Table III (the iodine is at the origin and the z direction is along the I–P bond). Unrestricted Hartree–Fock (UHF) and second-order Møller–Plesset perturbation theory (UMP2), as implemented in Gaussian 16,[51] is used to determine the ground state of the unpaired spin (i.e., the trapped electron) in this cluster. With this electron included, the net charge of the cluster is −5 and the spin multiplicity is 2. Geometry optimization is not done. The dgdzvp basis set (double zeta valence plus polarization) is used.[52] Yurieva *et al.*[53] and Siiskonen and Priimagi[54] showed that this basis set performs well for iodine. Table IV includes the calculated Fermi contact parameters, the Mulliken charges, and the spin densities for the eight ions in the $(IPS_6)^{5-}$ cluster, and Fig. 5 shows the results from Gaussian 16 for the distribution of spin density.

The Fermi contact parameters for the ^{127}I and ^{31}P nuclei in Table IV provide the most direct evidence that the $(IPS_6)^{5-}$ unit is the correct model for our iodine-related EPR spectrum. For the ^{31}P nucleus, the calculated value of 1815 MHz is very close to the experimental value of 1769 MHz, with the difference being only 2.6%. For the ^{127}I nucleus, the calculated value of 760 MHz is approximately a factor of 2 greater than the experimental value of 386 MHz. This latter result is encouraging, especially when considering the challenge of calculating the Fermi contact values for heavy ions such as iodine where relativistic effects are important.[55] Although the predicted Fermi contact parameters for the six sulfur nuclei are all small in Table IV, the values for S2 and S5 are larger than the other four values. These are the two sulfur ions (S2 and S5) that are farthest apart and are seen in the upper right and lower left portions of Fig. 5.

TABLE IV. Results from quantum chemistry modeling of the $(IPS_6)^{5-}$ cluster. These Fermi contact parameters, Mulliken charges, and spin densities are taken from the output of a UHF/UMP2 calculation performed using Gaussian 16. Units for the Fermi contact values are MHz.

Ion	Fermi contact	Mulliken charge	Spin density
I	759.6	0.2796	0.1847
P	1815.3	0.3920	0.3342
S1	−23.9	−0.9490	−0.0257
S2	134.2	−0.9281	0.1777
S3	−9.5	−0.9531	−0.0532
S4	23.3	−0.9323	0.0841
S5	178.5	−1.0233	0.2848
S6	4.1	−0.8858	0.0134

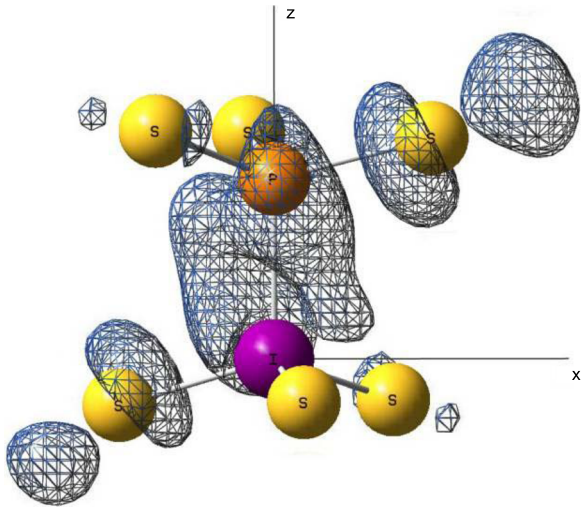

FIG. 5. Spin density distribution obtained from the quantum chemistry modeling (UHF/UMP2) of the $(IPS_6)^{5-}$ molecule. An isosurface cut-off value of 0.003 is used. Iodine is purple, phosphorus is orange, and sulfur is yellow.

The predicted spin densities in Table IV are also informative. They agree, in large part, with the earlier results in Sec. IV C, where the distribution of the spin in *s* and *p* orbitals was estimated using the experimental spin-Hamiltonian parameters. The predicted value of 0.1847 in Table IV for the spin density at the iodine ion is close to the estimate of 20%. The predicted values of 0.3342 for the phosphorous ion and 0.4811 for the sum of the sulfur ions in Table IV are not significantly different from the estimates of 50% and 30%, respectively.

Future computational efforts using advanced quantum chemistry modeling methods and a more versatile basis set are expected to provide a complete set of precise spin-Hamiltonian parameters for an $(IPS_6)^{5-}$ molecular ion embedded in an SPS crystal. These results, when compared to the present experimental spin-Hamiltonian parameters, will allow the model for our EPR-active iodine defect to be further refined by including spin-density sharing with Sn ions as well as relaxation effects (i.e., small shifts in the relative positions of ions within the molecular unit).

VI. SUMMARY

An electron-trapping defect responsible for an iodine-related EPR spectrum in ferroelectric and photorefractive $Sn_2P_2S_6$ crystals

has been identified. Iodine enters the photorefractive crystal as an unintentional impurity during growth by the chemical vapor transport method (when SnI_4 is used as the carrier gas). It substitutes for a phosphorous ion in a constituent $(P_2S_6)^{4-}$ anion and produces $(IPS_6)^{4-}$ units. Paramagnetic $(IPS_6)^{5-}$ units are then formed in the crystal when electrons are trapped at the $(IPS_6)^{4-}$ units after an exposure at 20 K to 633 nm laser light and the subsequent release of electrons from Te-associated defects upon warming to 100 K. The angular dependence of the EPR spectrum provides a complete set of spin-Hamiltonian parameters describing the g matrix and the ^{127}I and ^{31}P hyperfine matrices. The experimental values for the isotropic Fermi contact and the anisotropic dipole–dipole interactions, extracted from these matrices, allow estimates to be made for the distribution of the unpaired spin on the phosphorous and iodine ions. Quantum chemistry modeling (UHF/UMP2), using a small cluster approach and a dgdzvp basis set, supports the $(IPS_6)^{5-}$ description of the trapped electron.

A primary focus of the present study has been to investigate charge trapping by defects in SPS crystals, with the goal of improving the photorefractive response of the material. Although many of the SPS crystals used in photorefractive studies have been grown by the chemical vapor transport method, there has been no mention thus far in the literature that iodine may have entered the crystals. This incorporation of iodine in significant concentrations is now shown to occur, and moreover, the isolated iodine ions are shown to serve as traps for electrons. Future studies are needed that explore the influence (positive or negative) of the iodine impurities on the photorefractive response of the SPS crystals. These studies should address the competing (or complementing) roles of intentional impurities, such as Sb and Te, unintentional native defects, such as sulfur and tin vacancies, and the iodine ions. If warranted, future growth procedures may need to be modified to minimize or maximize the amount of iodine taken up by an SPS crystal.

ACKNOWLEDGMENTS

Work at the Air Force Research Laboratory was supported under Contract No. FA8650-16-D-5404 from the Air Force Office of Scientific Research. Work performed at Uzhhorod National University was supported by the Science and Technology Center of Ukraine and the European Office of Aerospace Research and Development (STCU/EOARD; Project No. P438b). The views expressed in this paper are those of the authors and do not necessarily reflect the official policy or position of the United States Air Force or the Department of Defense.

DATA AVAILABILITY

The data that support the findings of this study are available within the article.

REFERENCES

[1] K. Z. Rushchanskii, Y. M. Vysochanskii, and D. Strauch, "Ferroelectricity, nonlinear dynamics, and relaxation effects in monoclinic $Sn_2P_2S_6$," Phys. Rev. Lett. **99**, 207601 (2007).

[2] M. Sotome, M. Nakamura, J. Fujioka, M. Ogino, Y. Kaneko, T. Morimoto, Y. Zhang, M. Kawasaki, N. Nagaosa, Y. Tokura, and N. Ogawa, "Ultrafast spectroscopy of shift-current in ferroelectric semiconductor $Sn_2P_2S_6$," Appl. Phys. Lett. **114**, 151101 (2019).

[3] V. Liubachko, A. Oleaga, A. Salazar, R. Yevych, A. Kohutych, and Y. Vysochanskii, "Phase diagram of ferroelectrics with tricritical and Lifshitz points at coupling between polar and antipolar fluctuations," Phys. Rev. B **101**, 224110 (2020).

[4] S. G. Odoulov, A. N. Shumelyuk, U. Hellwig, R. A. Rupp, A. A. Grabar, and I. M. Stoyka, "Photorefraction in tin hypothiodiphosphate in the near infrared," J. Opt. Soc. Am. B **13**, 2352 (1996).

[5] S. G. Odoulov, A. N. Shumelyuk, U. Hellwig, R. A. Rupp, and A. A. Grabar, "Photorefractive beam coupling in tin hypothiodiphosphate in the near infrared," Opt. Lett. **21**, 752 (1996).

[6] S. G. Odoulov, A. N. Shumelyuk, G. A. Brost, and K. M. Magde, "Enhancement of beam coupling in the near infrared for tin hypothiophosphate," Appl. Phys. Lett. **69**, 3665 (1996).

[7] M. Jazbinšek, G. Montemezzani, P. Günter, A. A. Grabar, I. M. Stoika, and Y. M. Vysochanskii, "Fast near-infrared self-pumped phase conjugation with photorefractive $Sn_2P_2S_6$," J. Opt. Soc. Am. B **20**, 1241 (2003).

[8] M. Jazbinšek, D. Haertle, G. Montemezzani, P. Günter, A. A. Grabar, I. M. Stoika, and Y. M. Vysochanskii, "Wavelength dependence of visible and near-infrared photorefraction and phase conjugation in $Sn_2P_2S_6$," J. Opt. Soc. Am. B **22**, 2459 (2005).

[9] A. A. Grabar, M. Jazbinšek, A. N. Shumelyuk, Y. M. Vysochanskii, G. Monemezzani, and P. Günter, "Photorefractive effects in $Sn_2P_2S_6$," in *Photorefractive Materials and Their Applications 2*, edited by P. Günter and J. P. Huignard (Springer, New York, 2007), Chap. 10.

[10] T. Bach, M. Jazbinšek, G. Montemezzani, P. Günter, A. A. Grabar, and Y. M. Vysochanskii, "Tailoring of infrared photorefractive properties of $Sn_2P_2S_6$ crystals by Te and Sb doping," J. Opt. Soc. Am. B **24**, 1535 (2007).

[11] B. Sturman, P. Mathey, H. R. Jauslin, S. Odoulov, and A. Shumelyuk, "Modeling of the photorefractive nonlinear response in $Sn_2P_2S_6$ crystals," J. Opt. Soc. Am. B **24**, 1303 (2007).

[12] A. Shumelyuk, A. Hryhorashchuk, S. Odoulov, and D. R. Evans, "Transient gain enhancement in photorefractive crystals with two types of movable charge carrier," Opt. Lett. **32**, 1959 (2007).

[13] D. R. Evans, A. Shuymelyuk, G. Cook, and S. Odoulov, "Secondary photorefractive centers in $Sn_2P_2S_6$:Sb crystals," Opt. Lett. **36**, 454 (2011).

[14] Y. Skrypka, A. Shumelyuk, S. Odoulov, S. Basun, and D. Evans, "Light induced absorption and optical sensitizing of $Sn_2P_2S_6$:Sb," Opt. Commun. **356**, 208 (2015).

[15] A. Regmi, I. Biaggio, and A. A. Grabar, "Optical determination of the charge carrier mobility in $Sn_2P_2S_6$," Appl. Phys. Lett. **109**, 182104 (2016).

[16] Y. Skrypka, A. Shumelyuk, S. Odoulov, S. Basun, and D. R. Evans, "Temporal dynamics of two-beam coupling and the origin of compensation photorefractive gratings in $Sn_2P_2S_6$:Sb," Opt. Mater. Express **7**, 1414 (2017).

[17] O. M. Shumelyuk, A. Yu. Volkov, Ya. M. Skrypka, L. E. Halliburton, N. C. Giles, C. A. Lenyk, S. A. Basun, A. A. Grabar, Yu. M. Vysochansky, S. G. Odoulov, and D. R. Evans, "Near-infrared-sensitive photorefractive $Sn_2P_2S_6$ crystals grown by the Bridgman method," J. Appl. Phys. **127**, 103103 (2020).

[18] J.-M. Spaeth and H. Overhof, *Point Defects in Semiconductors and Insulators: Determination of Atomic and Electronic Structure from Paramagnetic Hyperfine Interactions* (Springer-Verlag, Berlin, 2003).

[19] J. A. Weil and J. R. Bolton, *Electron Paramagnetic Resonance: Elementary Theory and Practical Applications*, 2nd ed. (John Wiley & Sons, Hoboken, NJ, 2007).

[20] A. van der Est, "Continuous-wave EPR," in *EPR Spectroscopy: Fundamentals and Methods*, edited by D. Goldfarb and S. Stoll (John Wiley & Sons, Chichester, UK, 2018), Chap. 1.

[21] A. T. Brant, L. E. Halliburton, N. C. Giles, S. A. Basun, A. A. Grabar, and D. R. Evans, "Intrinsic small polarons (Sn^{3+} ions) in photorefractive $Sn_2P_2S_6$ crystals," J. Phys.: Condens. Matter **25**, 205501 (2013).

[22] E. M. Golden, S. A. Basun, A. A. Grabar, I. M. Stoika, N. C. Giles, D. R. Evans, and L. E. Halliburton, "Sulfur vacancies in photorefractive $Sn_2P_2S_6$ crystals," J. Appl. Phys. **116**, 244107 (2014).

[23] E. M. Golden, S. A. Basun, D. R. Evans, A. A. Grabar, I. M. Stoika, N. C. Giles, and L. E. Halliburton, "Sn vacancies in photorefractive $Sn_2P_2S_6$ crystals: An electron paramagnetic resonance study of an optically active hole trap," J. Appl. Phys. **120**, 133101 (2016).

[24]A. T. Brant, L. E. Halliburton, S. A. Basun, A. A. Grabar, S. G. Odoulov, A. Shumelyuk, N. C. Giles, and D. R. Evans, "Photoinduced EPR study of Sb^{2+} ions in photorefractive $Sn_2P_2S_6$ crystals," Phys. Rev. B **86**, 134109 (2012).
[25]B. E. Kananen, E. M. Golden, S. A. Basun, D. R. Evans, A. A. Grabar, I. M. Stoika, J. W. McClory, N. C. Giles, and L. E. Halliburton, "Dual role of Sb ions as electron traps and hole traps in photorefractive $Sn_2P_2S_6$ crystals," Opt. Mater. Express **6**, 3992 (2016).
[26]S. A. Basun, L. E. Halliburton, and D. R. Evans, "Hyperbolic decay of photo-created Sb^{2+} ions in $Sn_2P_2S_6$:Sb crystals detected with electron paramagnetic resonance," Appl. Phys. Lett. **110**, 052903 (2017).
[27]M. Bennati, "EPR interactions—Hyperfine couplings," in *EPR Spectroscopy: Fundamentals and Methods*, edited by D. Goldfarb and S. Stoll (John Wiley & Sons, Chichester, UK, 2018), Chap. 5.
[28]E. M. Scherrer, "Optical and electron paramagnetic resonance characterization of point defects in semiconductors," Ph.D. dissertation (Air Force Institute of Technology, Wright-Patterson Air Force Base, Dayton, OH, 2019), available at https://apps.dtic.mil/sti/citations/AD1078209.
[29]G. Dittmar and H. Schäfer, "The crystal structure of $Sn_2P_2S_6$," Z. Naturforsch. B **29**, 312 (1974).
[30]B. Scott, M. Pressprich, R. D. Willet, and D. A. Cleary, "High-temperature crystal-structure and DSC of $Sn_2P_2S_6$," J. Solid State Chem. **96**, 294 (1992).
[31]K. Kuepper, B. Schneider, V. Caciuc, M. Neumann, A. V. Postnikov, A. Ruediger, A. A. Grabar, and Y. M. Vysochanskii, "Electronic structure of $Sn_2P_2S_6$," Phys. Rev. B **67**, 115101 (2003).
[32]T. Babuka, K. Glukhov, Y. Vysochanskii, and M. Makowska-Janusik, "New insight into strong correlated states realised in a ferroelectric and paraelectric chalcogenide $Sn_2P_2S_6$ crystal," RSC Adv. **7**, 27770 (2017).
[33]K. Glukhov, K. Fedyo, J. Banys, and Y. Vysochanskii, "Electronic structure and phase transition in ferroelectric $Sn_2P_2S_6$ crystal," Int. J. Mol. Sci. **13**, 14356 (2012).
[34]A. A. Grabar, I. V. Kedyk, M. I. Gurzan, I. M. Stoika, A. A. Molnar, and Yu. M. Vysochanskii, "Enhanced photorefractive properties of modified $Sn_2P_2S_6$," Opt. Commun. **188**, 187 (2001).
[35]V. Shvalya, J. Zavašnik, V. Nasretdinova, H. Uršič, J. Kovač, A. Grabar, A. Kohutych, A. Molnar, D. R. Evans, D. D. Mihailović, and U. Cvelbar, "Customization of $Sn_2P_2S_6$ ferroelectrics by post-growth solid-state diffusion doping," J. Mater. Chem. C **8**, 9975 (2020).
[36]S. G. Parker, "Single crystals and epitaxial films of ZnSe by chemical transport," J. Cryst. Growth **9**, 177 (1971).
[37]S. Fujiwara, Y. Namikawa, M. Irikura, K. Matsumoto, T. Kotani, and T. Nakamura, "Growth of dislocation-free ZnSe single crystal by CVT method," J. Cryst. Growth **219**, 353 (2000).
[38]R. V. Gamernyk, Yu. P. Gnatenko, P. M. Bukivskij, P. A. Skubenko, and V. Yu. Slivka, "Optical and photoelectric spectroscopy of photorefractive $Sn_2P_2S_6$ crystals," J. Phys.: Condens. Matter **18**, 5323 (2006).
[39]A. Rüdiger, "Light induced charge transfer processes and pyroelectric luminescence in $Sn_2P_2S_6$," Ph.D. dissertation (University of Osnabrück, Osnabrück, Germany, 2001), p. 35, available at https://nbn-resolving.org/urn:nbn:de:gbv:700-2001092814.
[40]J. R. Morton and K. F. Preston, "Atomic parameters for paramagnetic resonance data," J. Magn. Reson. **30**, 577 (1978).
[41]J. A. J. Fitzpatrick, F. R. Manby, and C. M. Western, "The interpretation of molecular magnetic hyperfine interactions," J. Chem. Phys. **122**, 084312 (2005).
[42]I. N. Geifman, I. V. Kozlova, U. M. Vysochanski, V. Ya. Kofman, and O. A. Mikailo, "Temperature dependence of Mn^{2+} EPR in $Sn_2P_2S_6$ near the phase transition," Appl. Magn. Reson. **2**, 435 (1991).
[43]A. Carrington, P. N. Dyer, and D. H. Levy, "Gas-phase electron resonance spectra of BrO and IO," J. Chem. Phys. **52**, 309 (1970).
[44]C. E. Bailey, "ESR study of the I^0 atom in HIO_3," J. Chem. Phys. **59**, 1599 (1973).
[45]M. Iwasaki, K. Toriyama, and H. Muto, "Electron spin resonance of ^{127}I atoms trapped in Xe matrices," J. Chem. Phys. **71**, 2853 (1979).
[46]J. R. Byberg, "ESR spectrum of IO_2," J. Chem. Phys. **85**, 4790 (1986).
[47]J. R. Byberg, "ESR spectrum of IO_4^{2-}," J. Chem. Phys. **86**, 6065 (1987).
[48]J. R. Byberg, "Addition of O^- to IO_4^- in a crystalline matrix: A pentacoordinated iodine (VIII) species studied by ESR and optical spectroscopy," J. Phys. Chem. **96**, 4220 (1992).
[49]A. T. Brant, S. Yang, N. C. Giles, M. Z. Iqbal, A. Manivannan, and L. E. Halliburton, "Oxygen vacancies adjacent to Cu^{2+} ions in TiO_2 (rutile) crystals," J. Appl. Phys. **109**, 073711 (2011).
[50]R. E. Alonso, A. Svane, C. O. Rodríguez, and N. E. Christensen, "Nuclear quadrupole moment determination of ^{35}Cl, ^{79}Br, and ^{127}I," Phys. Rev. B **69**, 125101 (2004).
[51]M. J. Frisch *et al.*, Gaussian 16, Revision B.01, Gaussian, Inc., Wallingford, CT, 2016.
[52]C. Sosa, J. Andzelm, B. C. Elkin, E. Wimmer, K. D. Dobbs, and D. A. Dixon, "A local density functional study of the structure and vibrational frequencies of molecular transition-metal compounds," J. Phys. Chem. **96**, 6630 (1992).
[53]A. G. Yurieva, O. Kh. Poleshchuk, and V. D. Filimonov, "Comparative analysis of a full-electron basis set and pseudopotential for the iodine atom in DFT quantum-chemical calculations of iodine-containing compounds," J. Struct. Chem. **49**, 548 (2008).
[54]A. Siiskonen and A. Priimagi, "Benchmarking DFT methods with small basis sets for the calculation of halogen-bond strengths," J. Mol. Model. **23**, 50 (2017).
[55]M. Filatov and D. Cremer, "Relativistically corrected hyperfine structure constants calculated with the regular approximation applied to correlation corrected *ab initio* theory," J. Chem. Phys. **121**, 5618 (2004).